Purely interfacial and highly tunable spin-orbit torque operating field-effect transistor in graphene doubly proximitized by two-dimensional magnet $Cr_2Ge_2Te_6$ and WS_2

Klaus Zollner,[1,*] Marko D. Petrović,[2,3] Kapildeb Dolui,[3] Petr Plecháč,[2] Branislav K. Nikolić,[3,†] and Jaroslav Fabian[1]

[1] *Institute for Theoretical Physics, University of Regensburg, 93040 Regensburg, Germany*
[2] *Department of Mathematical Sciences, University of Delaware, Newark, DE 19716, USA*
[3] *Department of Physics and Astronomy, University of Delaware, Newark, DE 19716, USA*

Using first-principles combined with quantum transport calculations, we predict that graphene sandwiched between insulating monolayers of $Cr_2Ge_2Te_6$ ferromagnet and WS_2 transition-metal dichalcogenide will exhibit spin-orbit torque (SOT) when unpolarized charge current is injected parallel to interfaces of $Cr_2Ge_2Te_6$/graphene/WS_2 van der Waals (vdW) heterostructure. Although graphene by itself is nonmagnetic and it has negligible spin-orbit coupling (SOC), both of which are required for the SOT phenomenon, $Cr_2Ge_2Te_6$ induces proximity magnetism into graphene while WS_2 concurrently imprints valley-Zeeman and Rashba SOCs in it. Unlike SOT on conventional metallic ferromagnets brought into contact with normal materials supplying strong SOC, the predicted SOT on such *doubly proximitized* graphene can be tuned by up to two orders of magnitude via combined top and back electrostatic gates. The vdW heterostructure also reveals how damping-like component of the SOT vector can arise purely from interfaces and, therefore, even in the absence of any spin Hall current from the bulk of a material with strong SOC. The SOT-driven dynamics of proximity magnetization moves it from out-of-plane to in-plane direction which opens a gap in graphene and leads to zero off current and diverging on/off ratio in such *SOT field-effect transistor*.

Introduction.—The recent discovery of atomically-thin magnets [1, 2] has opened new avenues for basic research [3, 4] on magnetism in the two-dimensional (2D) limit, stabilized by anisotropies, as well as for applications in spintronics [5–9]. The family of van der Waals (vdW) layered magnetic materials includes both conductors (such as Fe_3GeTe_2) and insulators (such as $Cr_2Ge_2Te_6$ and CrI_3), as well as ferromagnets (such as Fe_3GeTe_2 and $Cr_2Ge_2Te_6$) and antiferromagnets (such as bilayer CrI_3) [3]. Unlike conventional bulk magnetic materials, monolayer or few layer magnets are sensitive to external manipulations—gating, straining and coupling to other 2D materials within vdW heterostructures—which can dramatically change their electronic structure and, therefore, the effective interactions between localized magnetic moments responsible for their long-range ordering.

In particular, very recent experiments have demonstrated spin-orbit torque (SOT) in Fe_3GeTe_2/Pt bilayers [8, 9] where Fe_3GeTe_2 brings perpendicular magnetic anisotropy (PMA) favorable for magnetization switching and gate-tunable Curie temperature (up to room temperature). The current-induced SOT [12, 13] is a phenomenon where unpolarized charge current injected parallel to the interface of ferromagnet/SO-coupled-material bilayers generates nonequilibrium spin density $\langle\hat{\mathbf{s}}\rangle_{\rm neq}(\mathbf{r})$ [14] within the ferromagnet which then exerts torque $\propto \langle\hat{\mathbf{s}}\rangle_{\rm neq}(\mathbf{r}) \times \mathbf{m}(\mathbf{r})$ on its local magnetization $\mathbf{m}(\mathbf{r})$ [15–19]. The SOT efficiency is optimized by using the smallest possible current density and minimal energy to reverse the magnetization direction from positive to negative z-axis perpendicular to the interface. Such SOT-operated devices are envisaged as building blocks of nonvolatile magnetic random access memories [20] or artificial neural networks [21]. However, thus fabricated Fe_3GeTe_2/Pt devices have employed ~ 10 nm thick Fe_3GeTe_2 layer while also passing current through the bulk of Pt and generating additional Joule heat losses (e.g., $\simeq 2.5 \times 10^{11}$ A/m^2 current density was used to switch magnetization of Fe_3GeTe_2 in Ref. [8], which is much higher than minimal $\simeq 6 \times 10^9$ A/m^2 achieved in ferromagnet/topological-insulator bilayers [22]). Thus, the ultimate goal in increasing efficiency of SOT, which could be achieved with all atomically-thin materials

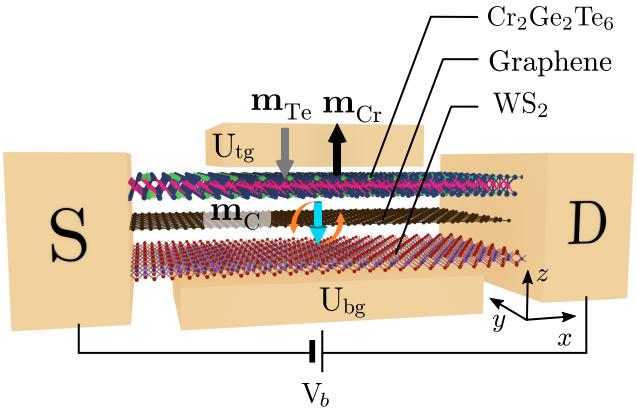

FIG. 1. Schematic view of $Cr_2Ge_2Te_6$/graphene/WS_2 vdW heterostructure which is attached to macroscopic source (S) and drain (D) reservoirs biased by a small bias voltage V_b which injected unpolarized charge current parallel to interfaces. A back gate voltage $U_{\rm bg}$ and a top gate voltage $U_{\rm tg}$ applied over smaller region [10] are assumed to control the Fermi energy and the local on-site potential in graphene, respectively. The unit vectors of magnetic moments on Cr, Te and C atoms are denoted by $\mathbf{m}_{\rm Cr}$, $\mathbf{m}_{\rm Te}$ and $\mathbf{m}_{\rm C}$, respectively, where only $\mathbf{m}_{\rm C}$ experiences SOT-driven dynamics.

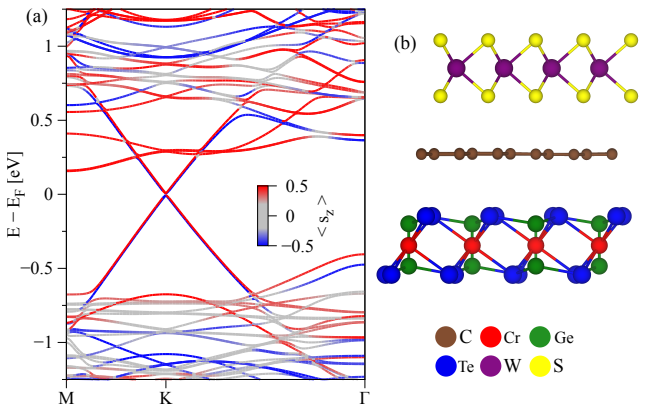

FIG. 2. (a) DFT-calculated electronic band structure of graphene sandwiched between monolayer $Cr_2Ge_2Te_6$ and monolayer WS_2. The color corresponds to the $\langle s_z \rangle$ expectation value in equilibrium. (b) Side view of the geometry of the trilayer supercell.

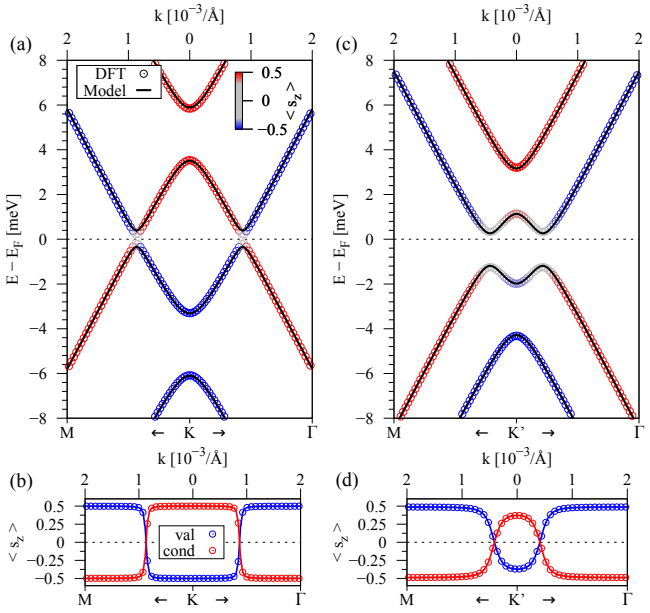

FIG. 3. (a) Zoom to the low energy bands around $E-E_F=0$ in Fig. 2. The Dirac cone is split by proximity induced exchange interaction and SOC. Color of the bands corresponds to $\langle s_z \rangle$ expectation value in equilibrium. (b) The $\langle s_z \rangle$ expectation value of the valence (conduction) band in blue (red). Symbols are first-principles computed data and solid lines are fit using the continuous model Hamiltonian [Eq. (1)]. (c),(d) The same information as in panels (a),(b), but for K′ point.

within vdW heterostructure offering atomically flat and highly transparent interfaces, remains to be realized.

In this Letter, we employ first-principles combined with quantum transport calculations to predict that vdW heterostructure $Cr_2Ge_2Te_6$/graphene/WS_2 composed of monolayer ferromagnetic insulator $Cr_2Ge_2Te_6$ [23], monolayer graphene and monolayer of insulating transition-metal dichalcogenide (TMD) WS_2 will exhibit SOT with greatly reduced Joule heat losses since current flows mostly through graphene. The proposed heterostructures differs from all previously explored ferromagnet/SO-coupled-material systems because graphene as material exhibiting SOT is neither magnetic nor SO-coupled (the intrinsic SOC in graphene is minuscule [24]) on its own. Instead, graphene within the vdW heterostructure depicted in Fig. 1 gets *proximitized from both sides* [25–29], where $Cr_2Ge_2Te_6$ induces exchange splitting while WS_2 induces SOC in graphene.

Furthermore, we demonstrate that SOT in graphene is *highly tunable*—it can be modulated by a factor $\sim$ 10–100 using transverse electric field due to the top and bottom gate voltages applied to the heterostructure illustrated in Fig. 1. This can be contrasted with previously achieved tuning of SOT by a factor of $\simeq$ 4 in ferromagnet/topological-insulator [30] or ferromagnet/TMD [31] bilayers. We assume that back gate and top gate will change the carrier density globally or locally, respectively, thereby making it possible to tune the Fermi energy of the whole device while concurrently creating a potential barrier within its smaller region, as demonstrated in previous experiments on graphene devices [10].

Finally, $Cr_2Ge_2Te_6$/graphene/WS_2 vdW heterostructure, *without* any bulk material and the SH current [32] generated by it, allows us to address a *key issue* [33, 34] in the field—*can purely interfacial-SOC-based mechanism generate damping-like (DL) component of SOT and how can such mechanism be controlled?* For example, DL SOT in Fe_3GeTe_2/Pt, or in conventional ferromagnet/heavy-metal bilayers, is standardly interpreted [8, 12] in terms of the spin Hall (SH) current flowing from the bulk of the heavy-metal layer (like Pt, Ta or W) into the ferromagnetic layer while traversing interface perpendicularly. Thus, its magnitude can hardly be controlled by external means and, instead, apparently requires to search for materials exhibiting the largest SH angle [32]. Moreover, experiments suggest [33] that interfacial SOC should be minimized because it generates spin memory loss [35] and, therefore, depolarization of SH current and reduction of the corresponding DL SOT. On the other hand, many experiments find opposite sign of field-like (FL) and DL components of the SOT vector—termed based on how they enter into the Landau-Lifshitz-Gilbert (LLG) equation for classical dynamics of magnetization where DL component is largely responsible [36] for magnetization switching [20]—thereby pointing to a single mechanism behind both SOT components [36]. Finally, recent first-principles quantum transport calculations [16, 17] for ferromagnet/heavy-metal bilayers have revealed an interfacial mechanism, not dependent on the thickness of the heavy metal layer and not yet fully understood microscopically, which generates DL SOT comparable or larger to the one expected from the SH current alone. This is in contrast to previous first-principles

TABLE I. The fitting parameters of model Hamiltonian $\hat{\mathcal{H}}$ in Eq. (1) for $Cr_2X_2Te_6$/graphene/WS_2 stacks with X = {Si, Ge, Te}. The values of parameters fit the DFT-computed bands both with and without SOC.

calc.	X	v_F [$10^5 \frac{m}{s}$]	Δ [meV]	λ_{ex}^A [meV]	λ_{ex}^B [meV]	λ_R [meV]	λ_I^A [meV]	λ_I^B [meV]	ξ [meV]	E_D [meV]
no SOC	Si	7.921	0.865	-1.899	-1.811	-	-	-	-	-0.012
no SOC	Ge	7.901	1.326	-3.644	-3.534	-	-	-	-	-0.054
no SOC	Sn	7.755	1.928	-6.483	-6.496	-	-	-	-	-0.053
SOC	Si	7.921	0.809	-1.964	-1.875	-0.397	1.127	-1.152	0.268	-0.758
SOC	Ge	7.903	1.252	-3.481	-3.650	-0.489	1.083	-1.118	0.244	-0.247
SOC	Sn	7.746	2.055	-6.281	-6.310	-0.696	1.009	-1.057	0.022	-0.610
no SOC [a]	Ge	7.979	1.602	-4.591	-4.422	-	-	-	-	0.008
SOC [a]	Ge	8.026	1.417	-4.566	-4.559	-0.467	1.148	-1.184	0.158	0.004

[a] Calculated with `WIEN2k` package [38], using the relaxed geometry from `Quantum ESPRESSO` package [37], and a k-point sampling of $12 \times 12 \times 1$. The cutoff is $RK_{max} = 4.0$ and the muffin-tin radii are $R_{Te} = 2.5$, $R_{Ge} = 2.25$, $R_{Cr} = 2.5$, $R_C = 1.36$, $R_W = 2.48$, and $R_S = 2.03$. The vdW corrections and a Hubbard $U = 1.0$ eV are also included.

calculations (utilizing phenomenological broadening η) which did not reveal any interfacial contribution to DL SOT [18, 19].

First-principles electronic and spin structure.—The density functional theory (DFT) calculations are performed on the supercell of $Cr_2Ge_2Te_6$/graphene/WS_2 stack depicted in Fig. 2(b) using `Quantum ESPRESSO` [37] and `WIEN2k` packages [38] packages, with details provided in the Supplemental Material (SM) [39]. This consists of a 5×5 supercell of graphene whose bottom surface is covered by a $\sqrt{3} \times \sqrt{3}$ supercell of $Cr_2Ge_2Te_6$, while its top surface is covered by a 4×4 supercell of WS_2. Bulk vdW crystal $Cr_2Ge_2Te_6$, which is composed of weakly bound monolayers, has Curie temperature $T_C \simeq 60$ K and PMA. Each monolayer is formed by edge-sharing $CrTe_6$ octahedra where Ge pairs are located in the hollow sites formed by the octahedra honeycomb. The layers are ABC-stacked, resulting in a rhombohedral $R\overline{3}$ symmetry. We stretch the lattice constant of graphene by roughly 2%—from 2.46 Å to 2.5 Å—and stretch the lattice constant of $Cr_2Ge_2Te_6$ by roughly 6%—from 6.8275 Å [45] to 7.2169 Å. The WS_2 lattice constant is compressed by roughly 1%—from 3.153 Å [46] to 3.125 Å. The heterostructure supercell has a lattice constant of 12.5 Å and it contains 128 atoms. The distance between WS_2 and graphene is $\simeq$ 3.28 Å, in agreement with previous calculations [27]. The distance between $Cr_2Ge_2Te_6$ and graphene is about 3.52 Å, also in agreement with previous calculations [47]. The band structure in Fig. 2(a) shows that the Dirac cone of graphene is preserved and located in the global band gap, so it can be probed by charge and spin transport. Figure 3 shows a zoom to the fine structure around K and K′ points with a fit to our continuous model Hamiltonian in Eq. (1).

Model Hamiltonian.—Using first-principles calculations and additional symmetry arguments [28, 48], we can extract a continuous model Hamiltonian

$$\hat{\mathcal{H}} = \hat{\mathcal{H}}_0 + \hat{\mathcal{H}}_\Delta + \hat{\mathcal{H}}_I + \hat{\mathcal{H}}_R + \hat{\mathcal{H}}_{ex} + \hat{\mathcal{H}}_\xi, \tag{1a}$$

$$\hat{\mathcal{H}}_0 = \hbar v_F(\tau k_x \hat{\sigma}_x - k_y \hat{\sigma}_y) \otimes \hat{s}_0, \tag{1b}$$

$$\hat{\mathcal{H}}_\Delta = \Delta \hat{\sigma}_z \otimes \hat{s}_0, \tag{1c}$$

$$\hat{\mathcal{H}}_I = \tau(\lambda_I^A \hat{\sigma}_+ + \lambda_I^B \hat{\sigma}_-) \otimes \hat{s}_z, \tag{1d}$$

$$\hat{\mathcal{H}}_R = -\lambda_R(\tau \hat{\sigma}_x \otimes \hat{s}_y + \hat{\sigma}_y \otimes \hat{s}_x), \tag{1e}$$

$$\hat{\mathcal{H}}_{ex} = (-\lambda_{ex}^A \hat{\sigma}_+ + \lambda_{ex}^B \hat{\sigma}_-) \otimes \hat{s}_z, \tag{1f}$$

$$\hat{\mathcal{H}}_\xi = \tau \xi \hat{\sigma}_0 \otimes \hat{s}_0, \tag{1g}$$

which is valid in the vicinity of both Dirac points, K and K′. The systems we consider have broken time-reversal symmetry and only C_3 symmetry. We denote v_F as the Fermi velocity, and wavevector components k_x and k_y are measured from ±K. The valley index is $\tau = \pm 1$ for ±K and the Pauli spin matrices are $\hat{s}_i$, acting on spin space $(\uparrow, \downarrow)$, and pseudospin matrices are $\hat{\sigma}_i$, acting on sublattice space (C_A, C_B), with $i = \{0, x, y, z\}$ where $i = 0$ denotes a unit 2×2 matrix. For notational convenience, we use $\hat{\sigma}_\pm = \frac{1}{2}(\hat{\sigma}_z \pm \hat{\sigma}_0)$. The staggered potential gap is Δ, and the parameters λ_I^A and λ_I^B denote the sublattice-resolved intrinsic SOC. The parameter λ_R is the Rashba SOC, and the proximity exchange interaction parameters are λ_{ex}^A and λ_{ex}^B. The parameter ξ describes valley exchange coupling resulting from an in-plane magnetization component [28]. The four basis states are $|\Psi_A, \uparrow\rangle$, $|\Psi_A, \downarrow\rangle$, $|\Psi_B, \uparrow\rangle$, and $|\Psi_B, \downarrow\rangle$. The model Hamiltonian is centered around the Fermi level at zero energy. Since first-principles results capture doping effects, we also introduce parameter E_D (termed Dirac point energy) which shifts the global band structure.

The fitting parameters for $Cr_2X_2Te_6$/graphene/WS_2 stacks with X = {Si,Ge,Te} are summarized in Table I. They are in agreement with previous calculations for graphene/TMD [26, 27] and graphene/$Cr_2Ge_2Te_6$ heterostructures [47]. As demonstrated by comparing symbols (DFT bands) and solid lines (model Hamiltonian

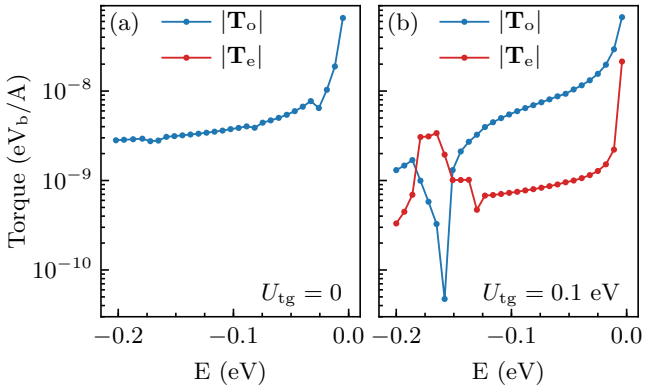

FIG. 4. The magnitude of odd $\mathbf{T}_o$ and even $\mathbf{T}_e$, in magnetization $\mathbf{m}_C$ of proximitized graphene, components of SOT vector versus the Fermi energy for $\mathbf{m}_C \parallel \mathbf{z}$: (a) without on-site potential $U_{tg} = 0$; and (b) with a constant on-site potential $U_{tg} = 0.1$ eV which creates a potential barrier and causes backscattering.

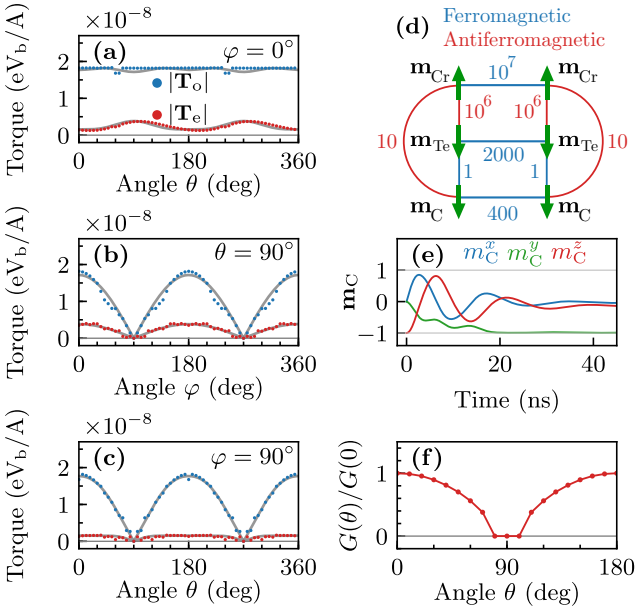

FIG. 5. (a)–(c) The angular dependence of SOT components $|\mathbf{T}_o|$ (blue dots) and $|\mathbf{T}_e|$ (red dots) from Fig. 4(b) for different orientations of magnetization $\mathbf{m}_C$ of proximitized graphene at $E_F = -0.02$ eV and with constant on-site potential $U_{tg} = 0.1$ eV in the central region. The vector $\mathbf{m}_C = (\sin\theta\cos\varphi, \sin\theta\sin\varphi, \cos\theta)$ is rotated within the xz-plane in (a); within the xy-plane in (b); and within the yz-plane in (c). Gray curves in the background show analytical fit to numerically calculated SOT values using Eq. (3). (d) DFT-computed exchange coupling constants between magnetic moments of Cr, Te and C atoms. (e) Classical dynamics of proximity magnetization $\mathbf{m}_C(t)$ of graphene which is exchange coupled to $\mathbf{m}_{Cr}$ and $\mathbf{m}_{Te}$ in panel (d) while experiencing SOT from panels (a)–(c). The dynamics is obtained by solving six coupled LLG equations for magnetic moments depicted in panel (d), where $\mathbf{m}_{Cr}(t)$ and $\mathbf{m}_{Te}(t)$ remain nearly fixed (so they are not plotted). (f) Normalized conductance of graphene as a function of angle θ as $\mathbf{m}_C$ moves due to SOT from out-of-plane ($\theta = 180°$) direction along the $-z$-axis to in-plane direction along the y-axis ($\theta = 90°$), in accord with panel (d).

bands) in Fig. 3, the model Hamiltonian in Eq. (1) with parameters from Table I can perfectly reproduce the band structure and $\langle \hat{s}_z \rangle$ expectation values around both valleys. The valley degeneracy is clearly broken, especially when looking at the highest (lowest) spin-up (spin-down) bands at the K and K′ valleys. This is due to the interplay of proximity exchange interaction and SOC, splitting the bands in the two valleys differently. Furthermore, Rashba SOC mixes the spin states and opens a global band gap, different for the two valleys. The SM [39] also provides equilibrium spin textures, band structure and fitting parameters for $Cr_2X_2Te_6$/graphene stacks without WS_2.

Quantum transport calculations of SOT.—First-principles quantum transport calculations of SOT in ferromagnet/heavy-metal bilayers have been previously conducted [18, 19] using the Kubo formula coupled to first-principles tight-binding (FPTB) Hamiltonians $\hat{H}_{FPTB}$, where one utilizes the retarded Green function (GF), $\hat{G}^r(E, k_x, k_y) = [E - \hat{H}_{FPTB}(k_x, k_y) + i\eta]^{-1}$, with phenomenological broadening η. However, this methodology cannot capture the full physics of SOT [60], and particularly its complex angular dependence [16, 17, 50]. Instead, we split infinite in the xy-plane (see coordinate system in Fig. 1) $Cr_2Ge_2Te_6$/graphene/WS_2 trilayer into semi-infinite left (L) lead, central region and semi-infinite right (R) lead of the Landauer setup for quantum transport calculations [51]. The leads are taken into account by the self-energies $\hat{\Sigma}_{L,R}(E, k_y)$. The simulated central region consists of an armchair graphene nanoribbon which is described by FPTB Hamiltonian $\hat{H}_{FPTB}$, corresponding to the continuous one in Eq. (1), which is written down explicitly in the SM [39]. The nanoribbon (illustrated in Fig. S4 in the SM [39]) is periodically repeated along the y-axis, so that k_y-points are sampled to take into account infinitely wide system [11].

The retarded GF of such central region is given by $\hat{G}^r(E, k_y) = [E - H_{FPTB}(k_y) - \hat{\Sigma}_L(E, k_y) - \hat{\Sigma}_R(E, k_y)]^{-1}$. By computing the nonequilibrium $\hat{\rho}_{neq}(k_y) = \frac{1}{2\pi i}\int dE\, \hat{G}^<(E, k_y)$ and the equilibrium $\hat{\rho}_{eq}(k_y) = -\frac{1}{\pi}\int dE\, \mathrm{Im}\, \hat{G}^r(E, k_y) f(E)$ density matrices—where we express lesser GF $\hat{G}^<(E)$ in terms of $\hat{G}^r(E, k_y)$ assuming elastic transport of electrons [51], and use Ozaki contour [52] for integral in $\hat{\rho}_{eq}(k_y)$ with $f(E)$ being the Fermi-Dirac distribution function—we can construct the current-driven (CD) part of the nonequilibrium density matrix $\hat{\rho}_{CD}(k_y) = \hat{\rho}(k_y)_{neq} - \hat{\rho}(k_y)_{eq}$ [15, 16]. This yields the CD *nonequilibrium* expectation value of spin density at site i, $\langle \hat{\mathbf{s}}_i \rangle_{CD}(k_y) = \frac{\hbar}{2}\mathrm{Tr}_{spin}[\hat{\rho}_{CD}(k_y)\hat{\mathbf{s}}]$, where the trace is performed in the spin space only. The k_y-dependent SOT is averaged over N_A atoms of the

triangular sublattice A and $N_{\rm B}$ atoms of the triangular sublattice B of the honeycomb lattice of graphene

$$\boldsymbol{\tau}(k_y) = \frac{1}{N_{\rm A}} \sum_{i\in {\rm A}} \left(-\frac{2\lambda_{\rm ex}^{\rm A}}{\hbar} \right) \langle \hat{\mathbf{s}}_i \rangle_{\rm CD}(k_y) \times \mathbf{m}_{\rm C} + \frac{1}{N_{\rm B}} \sum_{j\in {\rm B}} \frac{2\lambda_{\rm ex}^{\rm B}}{\hbar} \langle \hat{\mathbf{s}}_j \rangle_{\rm CD}(k_y) \times \mathbf{m}_{\rm C}, \tag{2}$$

as well as over the first Brillouin zone (BZ), $\mathbf{T} = \frac{W}{2\pi} \int_{\rm BZ} \boldsymbol{\tau}(k_y) dk_y$, where W is the width of the nanoribbon [Fig. S4 in the SM [39]]. This gives the magnitude of SOT components plotted in Figs. 4 and 5 in the units of eV_b/A, where V_b is the applied small bias voltage in the linear-response transport regime driving the injected current and A is the area of a single hexagon of the honeycomb lattice. The unit vector $\mathbf{m}_{\rm C} = (\sin\theta\cos\varphi, \sin\theta\sin\varphi, \cos\theta)$ specifies the direction of local magnetic moments on carbon atoms of both graphene sublattices.

The SOT vector can be decomposed, $\mathbf{T} = \mathbf{T}_{\rm o} + \mathbf{T}_{\rm e}$, into odd (o) and even (e) in $\mathbf{m}_{\rm C}$ components [18, 50]. Their Fermi energy dependence for $\mathbf{m}_{\rm C} \parallel \mathbf{z}$ ($\mathbf{z}$ is the unit vector along the z-axis) is shown in Fig. 4. Interpretation of experimental [50] and computational [16, 17] data for SOT requires to explain often observed complex angular dependence of $\mathbf{T}_{\rm o}$ and $\mathbf{T}_{\rm e}$. For this purpose, we fit computational data (dots) in Fig. 5(a)–(c) with an infinite series [16, 50] for $\mathbf{T}_{\rm e}$ and $\mathbf{T}_{\rm o}$ vector fields on the unit sphere of orientations of $\mathbf{m}_{\rm C}$. In the ballistic transport limit—with no impurities, potential barrier and, therefore, no voltage drop—$\mathbf{T}_{\rm e} \equiv 0$ in Fig. 4(a), as observed previously for simplistic Rashba ferromagnetic model [53]. In the same regime, $\mathbf{T}_{\rm o} = \tau_0\, \mathbf{y} \times \mathbf{m}_{\rm C}$ fits perfectly computational data, so that only the lowest order term of the series is needed and it acts as the pure FL SOT. It originates solely from the inverse spin-galvanic effect [54, 55] in which nonequilibrium spin density along the y-axis (with unit vector $\mathbf{y}$) arises due to unpolarized charge current injected along the x-axis in the presence of SOC-generated equilibrium spin textures (Fig. S1 in the SM [39]) and the corresponding spin-momentum locking.

Once the potential barrier is introduced into the graphene by using the top gate voltage to create a uniform on-site potential, $U_{\rm tg} = 0.1$ eV, a nonzero $\mathbf{T}_{\rm e} \neq 0$ emerges in Fig. 4(b) while both even and odd SOT components acquire complex angular dependences in Fig. 5(a)–(c). They can be fitted by

$$\mathbf{T}_{\rm o} = \left[\tau_0^{\rm o} + \tau_2^{\rm o} |\mathbf{z}\times\mathbf{m}_{\rm C}|^2 + \tau_4^{\rm o} |\mathbf{z}\times\mathbf{m}_{\rm C}|^4\right] (\mathbf{y}\times\mathbf{m}_{\rm C}), \tag{3a}$$

$$\mathbf{T}_{\rm e} = \left[\tau_0^{\rm e} + \tau_2^{\rm e} |\mathbf{z}\times\mathbf{m}_{\rm C}|^2 + \tau_4^{\rm e} |\mathbf{z}\times\mathbf{m}_{\rm C}|^4\right] \mathbf{m}_{\rm C}\times(\mathbf{y}\times\mathbf{m}_{\rm C}), \tag{3b}$$

with the numerical values of the fitting parameters given in the SM [39] (other expansions, such as using orthonormal vector spherical harmonics, can also be employed [17]). The lowest order term, $\mathbf{T}_{\rm e} = \tau_0^{\rm e} \mathbf{m}_{\rm C} \times (\mathbf{y} \times \mathbf{m}_{\rm C})$, is the standard DL SOT, while higher terms have properties of both FL and DL components [17].

The potential $U_{\rm tg} \neq 0$ that leads to nonzero $\mathbf{T}_{\rm e} \neq 0$ also generates reflection of electrons from such barrier. We fix its height at $U_{\rm tg} = 0.1$ eV in order to bring graphene into the so-called pseudodiffusive [56, 57] transport regime characterized by the same shot noise [58] as the diffusive wires with impurities (but no impurities are used in our clean proximitized graphene). Thus, Figs. 4(b) and 5(a)–(c) reveal that an interfacial mechanism for the DL SOT in proximitized graphene *requires* combination of SOC and back-scattering. Previously discussed mechanisms of purely interfacial generation of DL SOT have invoked either spin-dependent impurities [59, 60] or nonzero voltage drop [53]. As demonstrated in Fig. 4(b), combined tunning of the Fermi level and potential barrier height can modulate $|\mathbf{T}_{\rm o}|$ in doubly proximitized graphene by two orders of magnitude and $|\mathbf{T}_{\rm e}|$ by an order of magnitude.

Finally, by combining $\mathbf{T} = F(\mathbf{m}_{\rm C})$ from Eq. (3) with the coupled LLG equations, $d\mathbf{m}_{\rm X}/dt = -\gamma \mathbf{m}_{\rm X} \times \mathbf{B}_{\rm X}^{\rm eff} + \lambda \mathbf{m}_{\rm X} \times d\mathbf{m}_{\rm X}/dt + \frac{\gamma}{\mu_{\rm X}} \mathbf{T}$, for six magnetic moments on Cr, Te, and C atoms, we obtain the time evolution of $\mathbf{m}_{\rm C}(t)$ in Fig. 5(e). Here γ is the gyromagnetic ratio; $\mathbf{B}_{\rm X}^{\rm eff} = -\frac{1}{\mu_{\rm X}} \partial\mathcal{H}/\partial\mathbf{m}_1$ is the effective magnetic field due to exchange interactions in the classical Heisenberg Hamiltonian (with anisotropy) with exchange couplings J_{X-Y} whose values obtained from DFT calculations are given in Fig. 5(d) in units of $J_{\rm C-Te}$; and $\lambda = 0.01$ is chosen as the Gilbert damping parameter. The trajectory $\mathbf{m}_{\rm C}(t)$ in Fig. 5(d) shows that SOT will drive proximity magnetization in graphene from out-of-plane direction along the $-z$-axis to in-plane direction along the y-axis ($\theta = 90^\circ$). This opens a enlarges the gap in Fig. 3 of graphene, thereby bringing transmission function [Fig. S5 in the SM [39]] and the corresponding conductance in Fig. 5(f) to zero thereby making doubly proximized graphene to act as SOT field-effect transistor (SOTFET). For a logical gate to operate, its transistor should undergo transitions between the "off" and the "on" states, where the "on"/"off" ratio for the transistor conductance should be as high as possible to provide a reliable gate operation. While zero off current is impossible to achieve in conventional field-effect transistors with manipulation of classical barriers, and very recent proposals for SOTFET estimate "on"/"off" ratio at 10^8, the SOTFET unveiled by Fig. 5(f) exhibits ideal diverging "on"/"off" ratio.

K. Z. and J. F. were supported by DFG SPP 1666, DFG SFB 1277. M. D. P. and P. P. were supported by ARO MURI Award No. W911NF-14-0247. B. K. N. was supported by DOE Grant No. de-sc0016380. The supercomputing time was provided by XSEDE, which is supported by NSF Grant No. ACI-1053575.

* klaus.zollner@physik.uni-regensburg.de
† bnikolic@udel.edu

[1] C. Gong *et al.*, Discovery of intrinsic ferromagnetism in two-dimensional van der Waals crystals, Nature **546**, 265 (2017).
[2] B. Huang *et al.*, Layer-dependent ferromagnetism in a van der Waals crystal down to the monolayer limit, Nature **546**, 270 (2017).
[3] M. Gibertini, M. Koperski, A. F. Morpurgo, and K. S. Novoselov, Magnetic 2D materials and heterostructures, Nat. Nanotech. **14**, 408 (2019).
[4] K. S. Burch, D. Mandrus, and J.-G. Park, Magnetism in two-dimensional van der Waals materials, Nature **563**, 47 (2018).
[5] D. L. Cortie, G. L. Causer, K. C. Rule, H. Fritzsche, W. Kreuzpaintner, and F. Klose, Two-dimensional magnets: Forgotten history and recent progress towards spintronic applications, Adv. Funct. Mater. 1901414 (2019).
[6] C. Gong and X. Zhang, Two-dimensional magnetic crystals and emergent heterostructure devices, Science **363**, eaav4450 (2019).
[7] H. Li, S. Ruan, and Y.-J. Zeng, Intrinsic van der waals magnetic materials from bulk to the 2D limit: New frontiers of spintronics, Adv. Mat. 1900065 (2019).
[8] M. Alghamdi, M. Lohmann, J. Li, P. R. Jothi, Q. Shao, M. Aldosary, T. Su, B. P. T. Fokwa, and J. Shi, Highly efficient spinorbit torque and switching of layered ferromagnet Fe_3GeTe_2, Nano Lett. **19**, 4400 (2019).
[9] X. Wang *et al.*, Current-driven magnetization switching in a van der Waals ferromagnet Fe_3GeTe_2, `arXiv:1902.05794` (2019).
[10] A. F. Young and P. Kim, Quantum interference and Klein tunnelling in graphene heterojunctions, Nat. Phys. **5**, 222 (2009).
[11] M.-H. Liu and K. Richter, Efficient quantum transport simulation for bulk graphene heterojunctions, Phys. Rev. B **86**, 115455 (2012).
[12] A. Manchon, I. M. Miron, T. Jungwirth, J. Sinova, J. Zelezný, A. Thiaville, K. Garello, and P. Gambardella, Current-induced spin-orbit torques in ferromagnetic and antiferromagnetic systems, Rev. Mod. Phys. **91**, 035004 (2019).
[13] R. Ramaswamy, J. M. Lee, K. Cai, and H. Yang, Recent advances in spin-orbit torques: Moving towards device applications, Appl. Phys. Rev. **5**, 031107 (2018).
[14] P.-H. Chang, T. Markussen, S. Smidstrup, K. Stokbro, and B. K. Nikolić, Nonequilibrium spin texture within a thin layer below the surface of current-carrying topological insulator Bi_2Se_3: A first-principles quantum transport study, Phys. Rev. B **92**, 201406(R) (2015).
[15] B. K. Nikolić, K. Dolui, M. Petrović, P. Plecháč, T. Markussen, and K. Stokbro, First-principles quantum transport modeling of spin-transfer and spin-orbit torques in magnetic multilayers, in *Handbook of Materials Modeling: Applications: Current and Emerging Materials*, edited by W. Andreoni and S. Yip (Springer, Cham, 2018); `arXiv:1801.05793`.
[16] K. D. Belashchenko, A. A. Kovalev, and M. van Schilfgaarde, First-principles calculation of spin-orbit torque in a Co/Pt bilayer, Phys. Rev. Mater. **3**, 011401 (2019).
[17] K. D. Belashchenko, A. A. Kovalev, and M. van Schilfgaarde, Interfacial contributions to spin-orbit torque and magnetoresistance in ferromagnet/heavy-metal bilayers, `arXiv:1908.02680` (2019).
[18] F. Freimuth, S. Blügel, and Y. Mokrousov, Spin-orbit torques in co/pt(111) and mn/w(001) magnetic bilayers from first principles, Phys. Rev. B **90**, 174423 (2014).
[19] F. Mahfouzi and N. Kioussis, First-principles study of the angular dependence of the spin-orbit torque in Pt/Co and Pd/Co bilayers, Phys. Rev. B **97**, 224426 (2018).
[20] N. Locatelli, V. Cros, and J. Grollier, Spin-torque building blocks, Nat. Mater. **13**, 11 (2014).
[21] W. A. Borders, H. Akima, S. Fukami, S. Moriya, S. Kurihara, Y. Horio, S. Sato, and H. Ohno, Analogue spinorbit torque device for artificial-neural-network-based associative memory operation, Appl. Phys. Expr. **10**, 013007 (2017).
[22] Y. Wang *et al.*, Room temperature magnetization switching in topological insulator-ferromagnet heterostructures by spin-orbit torques, Nat. Commun. **8**, 1364 (2017).
[23] G. Menichetti, M. Calandra, and M. Polini, Electronic structure and magnetic properties of few-layer $Cr_2Ge_2Te_6$: The key role of nonlocal electron-electron interaction effects, 2D Mater. **6**, 045042 (2019).
[24] M. Gmitra, S. Konschuh, C. Ertler, C. Ambrosch-Draxl, and J. Fabian, Band-structure topologies of graphene: Spin-orbit coupling effects from first principles, Phys. Rev. B **80**, 235431 (2009).
[25] H. X. Yang, A. Hallal, D. Terrade, X. Waintal, S. Roche, and M. Chshiev, Proximity effects induced in graphene by magnetic insulators: First-principles calculations on spin filtering and exchange-splitting gaps, Phys. Rev. Lett. **110**, 046603 (2013).
[26] M. Gmitra and J. Fabian, Graphene on transition-metal dichalcogenides: A platform for proximity spin-orbit physics and optospintronics, Phys. Rev. B **92**, 155403 (2015).
[27] M. Gmitra, D. Kochan, P. Högl, and J. Fabian, Trivial and inverted Dirac bands and the emergence of quantum spin Hall states in graphene on transition-metal dichalcogenides, Phys. Rev. B **93**, 155104 (2016).
[28] V. T. Phong, N. R. Walet, and F. Guinea, Effective interactions in a graphene layer induced by the proximity to a ferromagnet, 2D Mater. **5**, 014004 (2017).
[29] I. Žutić, A. Matos-Abiague, B. Scharf, H. Dery, and K. Belashchenko, Proximitized materials, Mater. Today **22**, 85 (2019).
[30] Y. Fan *et al.*, Electric-field control of spin-orbit torque in a magnetically doped topological insulator, Nat. Nanotech. **11**, 352 (2016).
[31] W. Lv, Z. Jia, B. Wang, Y. Lu, X. Luo, B. Zhang, Z. Zeng, and Z. Liu, Electric-field control of spinorbit torques in WS_2/Permalloy bilayers, ACS Appl. Mater. Interfaces, **10**, 2843 (2018).
[32] J. Sinova, S. O. Valenzuela, J. Wunderlich, C. H. Back, and T. Jungwirth, Spin Hall effects, Rev. Mod. Phys. **87**, 1213 (2015).
[33] L. Zhu, D. C. Ralph, and R. A. Buhrman, Spin-orbit torques in heavy-metal–ferromagnet bilayers with varying strengths of interfacial spin-orbit coupling, Phys. Rev. Lett. **122**, 077201 (2019).
[34] K.-W. Kim, K.-J. Lee, J. Sinova, H.-W. Lee, and M.D. Stiles, Spin-orbit torques from interfacial spin-orbit coupling for various interfaces, Phys. Rev. B **96**, 104438 (2017).

[35] K. Dolui and B. K. Nikolić, Spin-memory loss due to spin-orbit coupling at ferromagnet/heavy-metal interfaces: *Ab initio* spin-density matrix approach, Phys. Rev. B **96**, 220403(R) (2017).

[36] J. Yoon, S.-W. Lee, J. H. Kwon, J. M. Lee, J. Son, X. Qiu, K.-J. Lee, and H. Yang, Anomalous spin-orbit torque switching due to field-like torque-assisted domain wall reflection, Sci. Adv. **3**, e1603099 (2017).

[37] P. Giannozzi *et al.*, QUANTUM ESPRESSO: A modular and open-source software project for quantum simulations of materials, J. Phys.: Condens. Mat. **21**, 395502 (2009).

[38] P. Blaha, K. Schwarz, G. K. H. Madsen, D. Kvasnicka, J. Luitz, R. Laskowski, F. Tran and L. D. Marks, *WIEN2k*, An Augmented Plane Wave + Local Orbitals Program for Calculating Crystal Properties (Karlheinz Schwarz, Techn. Universität Wien, Austria), 2018. ISBN 3-9501031-1-2

[39] See Supplemental Material at `https://wiki.physics.udel.edu/qttg/Publications` (which includes Refs. [40–44]) for the details of DFT calculations; equilibrium spin textures; band structure and fitting parameters for $Cr_2X_2Te_6$/graphene stacks without WS_2; and details of first-principles tight-binding Hamiltonian employed in quantum transport calculations.

[40] G. Kresse and D. Joubert, From ultrasoft pseudopotentials to the projector augmented-wave method, Phys. Rev. B **59**, 1758 (1999).

[41] J. P. Perdew, K. Burke, and M. Ernzerhof, Generalized gradient approximation made simple, Phys. Rev. Lett. **77**, 3865 (1996).

[42] S. Grimme, Semiempirical GGA-type density functional constructed with a long-range dispersion correction, J. Comput. Chem. **27**, 1787 (2006).

[43] V. Barone, M. Casarin, D. Forrer, M. Pavone, M. Sambi, and A. Vittadini, Role and effective treatment of dispersive forces in materials: Polyethylene and graphite crystals as test cases, J. Comput. Chem. **30**, 934 (2009).

[44] A. Manchon, H. C. Koo, J. Nitta, S. M. Frolov, and R. A. Duine, New perspectives for Rashba spin-orbit coupling, Nat. Mater. **14**, 871 (2015).

[45] V. Carteaux, D. Brunet, G. Ouvrard, and G. Andre, Crystallographic, magnetic and electronic structures of a new layered ferromagnetic compound $Cr_2Ge_2Te_6$, J. Phys.: Condens. Mat. **7**, 69 (1995).

[46] W. J. Schutte, J. L. De Boer, and F. Jellinek, Crystal structures of tungsten disulfide and diselenide, J. Solid State Chem. **70**, 207 (1987).

[47] J. Zhang, B. Zhao, Y. Yao, and Z. Yang, Robust quantum anomalous Hall effect in graphene-based van der Waals heterostructures, Phys. Rev. B **92**, 165418 (2015).

[48] D. Kochan, S. Irmer, and J. Fabian, Model spin-orbit coupling hamiltonians for graphene systems, Phys. Rev. B **95**, 165415 (2017).

[49] I. A. Ado, O. A. Tretiakov, and M. Titov, Microscopic theory of spin-orbit torques in two dimensions, Phys. Rev. B **95**, 094401 (2017).

[50] K. Garello, I. M. Miron, C. O. Avci, F. Freimuth, Y. Mokrousov, S. Blügel, S. Auffret, O. Boulle, G. Gaudin, and P. Gambardella, Symmetry and magnitude of spin-orbit torques in ferromagnetic heterostructures, Nat. Nanotech. **8**, 587 (2013).

[51] G. Stefanucci and R. van Leeuwen, *Nonequilibrium Many-Body Theory of Quantum Systems: A Modern Introduction* (Cambridge University Press, Cambridge, 2013).

[52] T. Ozaki, Continued fraction representation of the Fermi-Dirac function for large-scale electronic structure calculations, Phys. Rev. B **75**, 035123 (2007).

[53] A. Kalitsov, S. A. Nikolaev, J. Velev, M. Chshiev, and O. Mryasov, Intrinsic spin-orbit torque in a single-domain nanomagnet, Phys. Rev. B **96**, 214430 (2017).

[54] V. Edelstein, Spin polarization of conduction electrons induced by electric current in two-dimensional asymmetric electron system, Solid State Commun. **73**, 233 (1990);

[55] A. G. Aronov and Y. B. Lyanda-Geller, Nuclear electric resonance and orientation of carrier spins by an electric field, JETP Lett. **50**, 431 (1989).

[56] J. Tworzydło, B. Trauzettel, M. Titov, A. Rycerz, and C. W. J. Beenakker, Sub-Poissonian shot noise in graphene, Phys. Rev. Lett. **96**, 246802 (2006).

[57] A. Cresti, G. Grosso, and G. P. Parravicini, Numerical study of electronic transport in gated graphene ribbons, Phys. Rev. B **76**, 205433 (2007).

[58] R. Danneau, F. Wu, M. F. Craciun, S. Russo, M. Y. Tomi, J. Salmilehto, A. F. Morpurgo, and P. J. Hakonen, Shot noise in ballistic graphene, Phys. Rev. Lett. **100**, 196802 (2008).

[59] D. A. Pesin and A. H. MacDonald, Quantum kinetic theory of current-induced torques in Rashba ferromagnets, Phys. Rev. B **86**, 014416 (2012).

[60] I. A. Ado, Oleg A. Tretiakov, and M. Titov, Microscopic theory of spin-orbit torques in two dimensions, Phys. Rev. B **95**, 094401 (2017).

[61] X. Li *al.*, Spin-orbit-torque field-effect transistor (SOTFET): A new magnetoelectric memory, `arXiv:1909.08133` (2019).